Nano Research

Open Access

Research Article

Design of magnetic metal-organic frameworks-molecularly imprinted polymer for extracting and microfluidic sensing of sulfamethoxazole

Ziyang Zhu[1,2], Gaowa Xing[2], Li Xue[2], Wanting Yan[2], Wanqing Hu[2], Jiawei Li[1], Zirui Wang[1], Zenghe Li[1] ✉, and Jin-Ming Lin[2] ✉

[1] College of Chemistry, Beijing University of Chemical Technology, Beijing 100029, China
[2] Beijing Key Laboratory of Microanalysis Methods and Instrumentation, Key Laboratory of Bioorganic Phosphorus Chemistry & Chemical Biology (Ministry of Education), Department of Chemistry, Tsinghua University, Beijing 100084, China

Cite this article: *Nano Research*, **2026**, *19*, 94908495. https://doi.org/10.26599/NR.2026.94908495

ABSTRACT: This study successfully designed and synthesized a novel magnetic molecularly imprinted composite material, Fe_3O_4@PCN-222@MIP, which integrates Fe_3O_4 nanoparticles, zirconium-based metal-organic framework (PCN-222), and molecularly imprinted polymer. This composite exhibits excellent magnetic responsiveness, high specific surface area, and characteristic recognition, enabling efficient enrichment and specific identification of sulfamethoxazole (SMX). The molecularly imprinted cavities provide complementary spatial structures and functional sites for SMX through hydrogen bonding and π–π interactions, achieving precise recognition. Notably, the composite also exhibits inherent peroxidase (POD)-like activity. Upon binding to SMX, electrons transfer from Fe to the sulfur atom in SMX, inhibiting its catalytic activity and reducing H_2O_2 decomposition efficiency, thereby establishing a direct colorimetric detection mechanism. We developed a microfluidic chip sensor integrating magnetic solid-phase extraction (MSPE) with colorimetric detection was developed. This method achieves a broad linear range (100–4200 nmol·L^{-1}) and low detection limit (632.74 nmol·L^{-1}) for SMX. When applied to complex food samples such as milk and honey, its recovery rates reaches 90%–110% without complex elution steps, demonstrating outstanding practicality and showing high consistency with high-performance liquid chromatography (HPLC). This study not only introduces innovative functional materials but also provides solutions for integrated, simplified equipment suitable for potential field applications.

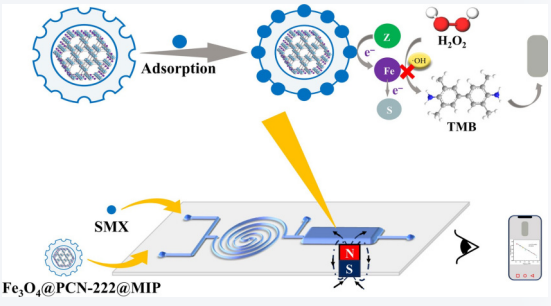

KEYWORDS: sulfamethoxazole, molecularly imprinted, sensor, microfluidic chip, colorimetric detection

1 Introduction

In recent years, the overuse of antibiotics in healthcare, livestock farming, and aquaculture has led to increasingly prominent residue issues in water bodies [1], soil [2], and food [3], posing a serious threat to the ecological environment and human health [4]. Sulfamethoxazole (SMX), a commonly used broad-spectrum sulfonamide antibiotic, due to its high water solubility and stability [5], tends to persist in the environment, promoting the emergence and spread of antibiotic-resistant bacteria, and may even pose potential risks to humans through the food chain [6]. Although traditional methods such as high-performance liquid chromatography (HPLC) [7] and mass spectrometry (MS) [8] offer high sensitivity, they rely on expensive equipment and complex sample pretreatment, making them unsuitable for rapid on-site screening [9]. Therefore, the development of efficient, low-cost, integrated materials that combine selective adsorption and sensitive detection capabilities has become a key direction in the field of environmental pollutant monitoring.

Metal-organic frameworks (MOFs) materials show great potential in the field of adsorption and separation due to their high specific surface area, tunable pore size and abundant active sites [10]. Among these, PCN-222 (also known as MOF-545) demonstrates outstanding adsorption performance toward SMX due to its excellent photochemical properties conferred by

Received: November 25, 2025; **Revised:** January 26, 2026
Accepted: January 27, 2026

✉Address correspondence to Zenghe Li, lizh@mail.buct.edu.cn; Jin-Ming Lin, jmlin@mail.tsinghua.edu.cn

porphyrin ligands and stable mesoporous structure [11, 12], making it an ideal carrier for functional materials [13]. However, single MOFs materials are difficult to separate quickly after adsorption and have limited ability to recognize specific target molecules [14]. To solve this problem, researchers often simplify the separation process by introducing magnetic nanoparticles (e.g., Fe_3O_4) to endow the materials with magnetic responsive properties [15]. Additionally, combining MOFs with molecularly imprinted polymers (MIPs) can significantly enhance the selective adsorption ability by constructing specific recognition cavities using template molecules [16]. MIPs can realize "lock-and-key" selective adsorption by inducing the formation of specific recognition sites through template molecules [17], but their traditional carriers (e.g., silica gel or polymer matrices) often suffer from the problems of low mechanical strength and slow mass transfer rate. The construction of and MIPs to construct MOF@MIP, on the one hand, the multilevel pore structure of MOFs can provide an orderly support platform for the imprinted layer, which can enhance the mass transfer efficiency and expose more active sites [18]; on the other hand, the precise recognition ability of MIPs can give the MOFs "smart" adsorption characteristics for the target pollutants, which can lead to "lock-and-key" selective adsorption [19]. On the other hand, the precise recognition ability of MIPs can provide MOFs with "smart" adsorption characteristics for target pollutants, thus realizing efficient separation and enrichment in complex environments [20]. However, the existing MOF@MIP usually need to elute the adsorbed drug for detection, with interference caused by human factors [21], and these methods require relatively expensive instruments and complicated pretreatment [22]. Therefore, the efficient integration of open and easy separation, high adsorption capacity and specific recognition function, and further combined with rapid detection means, remains an urgent technical challenge to be broken through.

In recent years, nanostructured materials, such as natural microfiber optical waveguides, have provided novel approaches for constructing highly sensitive sensing interfaces [23]. Colorimetric sensing technology is favored in the field of environmental testing due to its advantages of easy operation, low cost and visual readout [24]. The enzyme-catalyzed colorimetric system using 3,3',5,5'-tetramethylbenzidine (TMB) as the chromogenic substrate and hydrogen peroxide (H_2O_2) as the oxidant is widely used in the design of peroxidase mimics due to the mild reaction conditions and the easy signal capture [25]. Fe_3O_4, as a traditional nanozyme, exhibits excellent peroxidase (POD) catalytic activity [26]. The composite of Fe_3O_4 and MOFs can significantly enhance the catalytic activity and promote the Fenton reaction [27, 28], which promotes the Fenton reaction and enhances the optical signal generated by the colorimetric reaction [29]. At the same time, the composite MIP on the surface of Fe_3O_4@MOFs can provide more active sites for adsorption of SMX, thus generating electronic interactions that enhance or weaken the catalytic activity of the magnetic material Fe_3O_4@MOF@MIP, resulting in the enhancement or weakening of the TMB color [30]. It provides the possibility of a colorimetric sensor for the detection of SMX using the magnetic material Fe_3O_4@MOF@MIP.

In this work, we constructed a substrate for magnetically driven separation of MOFs (Fe_3O_4@PCN-222) by surface modification of Fe_3O_4 nanoparticles on Zr-MOF (PCN-222) by ball milling; subsequently, the molecularly imprinted material Fe_3O_4@PCN-222@MIP was constructed on the surface of sulfamethoxazole as a template molecule (Schemes 1(a) and 1(b)). This material has the functions of separation, enrichment and detection at the same time, and can selectively enrich SMX antibiotics through the specific recognition site of MIP itself. An on-chip MIP magnetic solid-phase extraction (MSPE) colorimetric assay based on a microfluidic approach was developed for the detection of SMX antibiotics in animal products based on the recognition of Fe_3O_4@PCN-222@MIP (Scheme 1(c)). When SMX was recognized by Fe_3O_4@PCN-222@MIP, the interaction between the functional groups on the surface of the material and the target was used to induce a colorimetric signal change, realizing the synergistic effect of adsorption and detection. The microfluidic chip integrated the whole detection process, including separation enrichment and detection. Under the optimal catalytic conditions, the system obtained a wide linear range (100–4200 nmol·L^{-1}) and a low detection limit (632.74 nmol·L^{-1}). The proposed on-chip MSPE-colorimetric analytical method allowed the rapid determination of milk and honey samples with results consistent with HPLC. This work provides an innovative solution for the targeted removal and sensitive detection of trace antibiotics in the environment, and expands the ideas for the design and application of multifunctional MOFs composites.

2 Experimental

2.1 Reagents and materials

Zirconium oxychloride octahydrate ($ZrOCl_2·H_2O$, 98%) was purchased from Shanghai Meryer Biochemistry Co. Ltd. (Shanghai, China). SMX (99%), sulfadiazine (SD, 99%), sulfamethazine (SDM, 98%), sodium acetate (NaAc, 99%), trifluoroacetic acid (TFA, 99.5%), methacrylic acid (MAA, 99%), and 4-vinyl pyridine (4-VP, 95%) were purchased from J&K Scientific Biochemicals Ltd. (Beijing, China). Meso-tetra(4-carboxyphenyl) porphin ($TCPP(H_2)$, 95%), acrylamide (AM, 99%), 4-vinylphenylboronic acid (4-VA, 96%), 2,2'-azobisisobutyronitrile (AIBN, 98%), and ethylene dimethacrylate (EGDMA, 98%) were purchased from Macklin Biochemicals (Shanghai, China). Ferric chloride hexahydrate ($FeCl_3·6H_2O$, 99%) was purchased from Tianjin Fuchen Biochemical Co. Ethylene glycol (EG, ≥ 99.0%), N,N-dimethylformamide (DMF, ≥ 99.5%), and acetic acid (HAC, ≥ 99.5%) were purchased from Tianjin Fuyu Biochemistry Co. Ltd. (Tianjin, China). Negative photoresist (SU-8 2050) and corresponding developer were purchased from Microchem Corporation (Newton, USA). Sylgard 184 poly(dimethyl siloxane) (PDMS) base and curing agent were bought from Dow Corning (Midland, MI, USA).

2.2 Apparatus

The morphology of Fe_3O_4@PCN-222@MIP was studied by scanning electron microscopy (SEM, ZEISS Sigma 360, Germany) and transmission electron microscopy (TEM, FEI Tecnai F20, USA). The crystal structure of Fe_3O_4@PCN-222@MIP was investigated by X-ray diffraction (XRD, Rigaku Smar Lab SE, Japan). Fourier transform infrared spectroscopy (FT-IR, Nicilet 6700, USA), and X-ray photoelectron spectroscopy (XPS, ESCALAB 250Xi, USA) were used to investigate the surface functional groups and molecular structure of Fe_3O_4@PCN-222@MIP. Thermogravimetric analyzer (TG, HITACHI STA200, Japan) was used to study the thermal stability and composition of

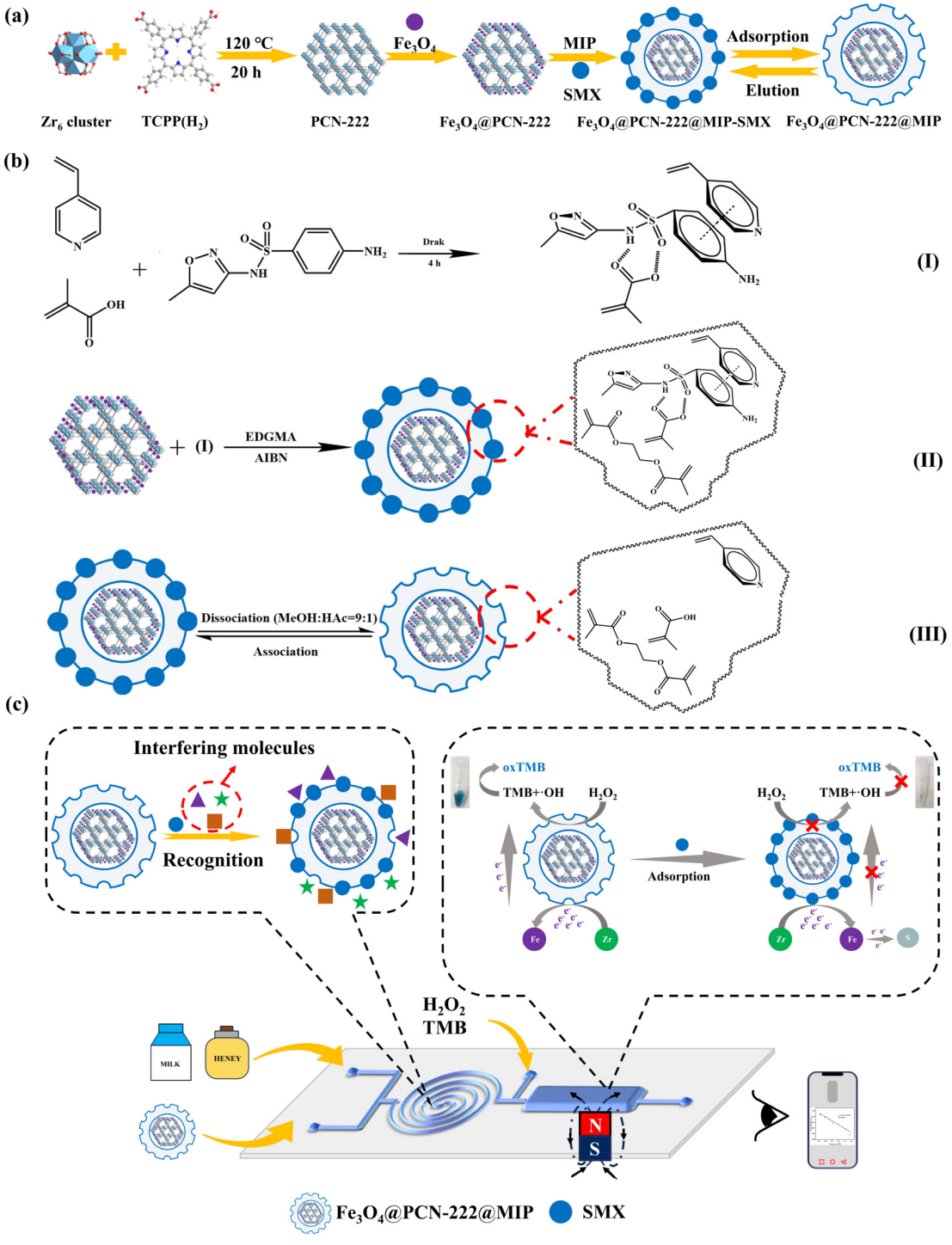

Scheme 1 Schematic of microfluidic magnetic solid-phase extraction-colorimetric method for separating and detecting SMX based on Fe_3O_4@PCN-222@MIP: (a) synthesis process of Fe_3O_4@PCN-222@MIP; (b) schematic of MIP binding and adsorption-desorption of Fe_3O_4@PCN-222@MIP with SMX; (c) schematic of SMX separation and detection.

Fe_3O_4@PCN-222@MIP. A vibrating sample magnetometer (VSM, Lake Shore 7404, USA) was used to characterize the magnetic properties of the materials. A gas adsorption meter (BET, Quanta chrome Nova 4000e, USA) was used to determine the specific surface area and pore size of the materials. Colorimetric assays were performed using an enzyme marker (Microplate Reader). Quantitative analysis of antibiotics was performed using Agilent 1260 Infinity II ultra-high liquid chromatography (HPLC, USA). Three-dimensional (3D) printer (full-color model: Stratasys J55) was purchased from Shanghai Liantai Technology Co., Ltd. (Shanghai, China), accuracy: 100 mm ± 0.1 mm.

2.3 Synthesis of Fe_3O_4@MOF@MIP

Fe_3O_4 magnetic particles were prepared by hydrothermal method, and the synthesis was improved according to the method in Ref. [31]. 1.35 g of $FeCl_3·6H_2O$ was dissolved in 50 mL of EG, and after

ultrasonication for 5 min, 3.6 g of NaAc was added. the mixture was then stirred for 30 min to obtain a homogeneous solution. The solution was transferred to a Teflon-lined stainless-steel autoclave. The autoclave was heated at 200 °C for 8 h and cooled to room temperature. The solid particles obtained were then washed three times with ethanol and water, respectively, and dried at 60 °C overnight.

Fe_3O_4@PCN-222 composites were prepared by ball milling method and the synthesis was improved according to the method in the literature [32, 33]. The PCN-222 material was first prepared by hydrothermal method [34]. 0.20 g of TCPP(H_2), 0.55 g of $ZrOCl_2{\cdot}8H_2O$, and 2.25 mL of trifluoroacetic acid (TFA) were dissolved in 50 mL of DMF and ultrasonically dissolved for 30 min to make the substances well dispersed. The homogeneous suspension was poured into a 100 mL Teflon liner and heated at 120 °C for 20 h. The product was washed with DMF and water sequentially and dried at 60 °C overnight. The Fe_3O_4@PCN-222 composite was then prepared by ball milling method. The Fe_3O_4@PCN-222 composites were obtained by ball milling Fe_3O_4 and PCN-222 (1:1, m:m) using zirconia balls with diameters of 1.5 and 1.0 mm at 500 rpm for 20 min.

Fe_3O_4@PCN-222@MIP composites were prepared by *in-situ* growth method, and the synthesis was improved according to the method in Refs. [35, 36]. 0.5 mmol of SMX and 2.00 mmol of a mixture of 4-VP and MAA (1:1, mol:mol) were fully dispersed in 50 mL of methanol and self-assembled in the dark at room temperature for 4 h. Then, 100 mg of Fe_3O_4@PCN-222, 5.0 mmol of EGDMA and 0.5 mmol of AIBN and sonicated for 15 min. after purging with N_2 for 10 min, the system was polymerized at 60 °C for 24 h. To remove SMX, the product was washed with methanol: acetic acid (9:1, V:V) until SMX was undetectable by HPLC and then dried at 60 °C overnight [37]. The synthesis conditions for Fe_3O_4@PCN-222@NIP are similar to those for Fe_3O_4@PCN-222@MIP, except that the template molecule SMX is not added. The imprinting factor (IF) is described by Eq. (1).

$$IF = \frac{Q_{MIP}}{Q_{NIP}} \tag{1}$$

where Q_{MIP} and Q_{NIP} (mg·L^{-1}) are the equilibrium adsorption capacities of Fe_3O_4@PCN-222@MIP and Fe_3O_4@PCN-222@NIP for SMX.

2.4 Adsorption isotherm fitting and adsorption kinetic fitting

The saturated adsorption capacity of Fe_3O_4@PCN-222@MIP was tested via static equilibrium experiments. Fe_3O_4@PCN-222@MIP and Fe_3O_4@PCN-222@NIP were placed in SMX solutions of different concentrations and shaken at room temperature for 2 h. After adsorption was complete, the supernatant was collected after centrifugation and analyzed by HPLC to determine the residual SMX content. The adsorption capacity (Q_e) was calculated using Eq. (1). Three parallel experiments were designed for each concentration, and the average values were calculated.

$$Q_e = \frac{(C_0 - C_e)\,V}{m} \tag{2}$$

where Q_e (mg·L^{-1}) represents the adsorption capacity of the SMX solution, C_0 (mg·L^{-1}) denotes the initial concentration of the SMX solution, C_e (mg·L^{-1}) indicates the equilibrium concentration of the SMX solution, V (L) signifies the volume, and m (g) represents the mass of Fe_3O_4@PCN-222@MIP or Fe_3O_4@PCN-222@NIP.

Adsorption kinetics experiments were conducted to measure the adsorption rate (20 mg·L^{-1}). Fe_3O_4@PCN-222@MIP or Fe_3O_4@PCN-222@NIP was added to 10.0 mL of a solution with a concentration of 20 mg·L^{-1} and adsorbed at room temperature for 5–180 min. Equations (3) and (4) were used to fit pseudo-first-order kinetic model and pseudo-second-order kinetic model for the adsorption of SMX by Fe_3O_4@PCN-222@MIP and Fe_3O_4@PCN-222@NIP [38].

Based on static adsorption data analysis, adsorption isotherm fitting was performed for Fe3O4@PCN-222@MIP or Fe_3O_4@PCN-222@NIP at different concentrations (5–200 mg·L^{-1}). The adsorption performance of the materials was studied using the Langmuir model (Eq. (5)) and Freundlich model (Eq. (6)) [39]. The Langmuir isotherm equation is suitable for describing the adsorption of an ideal monolayer on a homogeneous surface of an adsorbent, and the Freundlich isotherm equation is suitable for describing multilayer adsorption with binding sites of different affinities.

$$\ln(Q_e - Q_t) = \ln Q_e - k_1 t \tag{3}$$

$$\frac{t}{Q_t} = \frac{1}{k_2 Q_e^2} + \frac{t}{Q_e} \tag{4}$$

$$\frac{C_e}{Q_e} = \frac{1}{Q_m K_L} + \frac{C_e}{Q_m} \tag{5}$$

$$\ln Q_e = \ln K_F + \frac{1}{n}\ln C_e \tag{6}$$

where Q_e (mg·g^{-1}) is the equilibrium adsorption capacity. Q_t (mg·g^{-1}) is the adsorption capacity of adsorbent at time t (min). k_1 (min^{-1}) and k_2 (g·mg^{-1}·min^{-}) are the pseudo-first-order rate constant and pseudo second-order rate constant. Q_m (mg·g^{-1}) is the maximum adsorption capacity, K_L is Langmuir's constant, K_F is Freundlich's constant, n is Freundlich's exponent, and n = 1 for irreversible adsorption, n > 1 for favorable adsorption, and n < 1 for opposite adsorption.

2.5 POD-like activity study of Fe_3O_4@PCN-222@MIP

The POD-like activity of Fe_3O_4@PCN-222@MIP was investigated by enzyme kinetic theory and methodology using H_2O_2 and TMB as substrates. Based on the Lineweaver–Burk plot of the Michaelis–Menten double inverse equation, the kinetic parameters can be calculated as follows (Eq. (7)) [40]

$$\frac{1}{v} = \frac{K_m}{V_{max}[S]} + \frac{1}{V_{max}} \tag{7}$$

where v is the initial velocity, V_{max} represents the maximum reaction velocity, K_m is the Michaelis–Menten constant, and [S] is the substrate concentration.

2.6 Design and fabrication of microfluidic chip

The microfluidic chip was fabricated using three-dimensional (3D) printing technology. As shown in (Scheme. 1(c)) and Fig. S1 in the Electronic Supplementary Material (ESM) [41], the chip measures (80 mm (L) × 50 mm (W) × 8 mm (H)) and comprises three main functional sections: (1) a micro-stirrer integrating two inlets and a convergent-divergent spiral structure for efficient mixing of

magnetic nanoparticles (MNPs) with samples and thorough incubation; (2) lateral sample ports for introducing H_2O_2, TMB, and buffer solutions; (3) a detection chamber to hold the mixed sample, enabling image acquisition and analysis via a proprietary smartphone application. During chip fabrication, a microfluidic channel mold was first designed and printed using a 3D printer. Subsequently, PDMS prepolymer and curing agent were mixed at a 10:1 mass ratio, poured into the mold, and cured at 65 °C for 12 h. After curing, the PDMS replica is peeled from the mold and placed alongside thoroughly cleaned glass slides in a plasma cleaner. Both are treated at 100 W power for 1 minute, immediately aligned and bonded, then heated on an 85 °C hot plate for 30 min to achieve irreversible chip encapsulation [42].

2.7 Visual detection of SMX

The colorimetric assay procedure for SMX is as follows: First, 100 μL of suspension containing 8 mg Fe_3O_4@PCN-222@MIP was taken. Then, 160 μL of 20 mmol·L^{-1} NaAc–HAc buffer (pH 3.5), 10 μL of 0.7 μmol·L^{-1} TMB solution, 10 μL of 5 mmol·L^{-1} H_2O_2 solution, and 20 μL of SMX solution at gradient concentrations (100–4200 nmol·L^{-1}) in a 96-well plate. The mixture was then incubated at 25 °C for 20 min. Colorimetric images were captured using a Huawei P30 smartphone fixed within a light-tight chamber at a 12 cm distance. Camera settings were fixed (exposure: 1/120 s, ISO: 100, white balance: 5500 K; autofocus and flash disabled). Experiments were performed in triplicate. Images were converted to grayscale, the central region of each well was cropped, and the average intensity was analyzed with ImageJ. Data were normalized against the SMX-free blank. For validation, we also measured the absorbance of the same plate was measured in parallel using a microplate reader.

2.8 On-chip MSPE and detection of SMX

An aqueous suspension containing 100 μL of 8.0 mg Fe_3O_4@PCN-222@MIP MNPs and 20 μL of SMX were injected into inlet 1 and 2, respectively, 10 μL of 0.7 μmol·L^{-1} TMB and 160 μL of 20 mmol·L^{-1} NaAc–HAc buffer solution (pH 3.5) into inlet 3, and 10 μL of 5 mmol·L^{-1} H_2O_2 into inlet 4 with a syringe pump. The above solutions were loaded into the microfluidic system with a syringe pump at a loading flow rate of 10 μL·min^{-1}. After flowing into the detection chamber, the MNPs were tightly fixed in the chamber with a permanent magnet. After 20 min incubation at 25 °C, visual detection (Section 2.7) was performed, and HPLC verified the integrated MSPE-colorimetric process.

2.9 Performance evaluation of Fe_3O_4@PCN-222@MIP sensor

The performance evaluation of the Fe_3O_4@PCN-222@MIP sensor encompasses specificity, sensitivity, repeatability, and applicability to real samples. Selectivity experiments were conducted using SD and sulfadimidine (SDZ) as structural analogues, and tetracycline (TC), doxycycline (DOX), oxytetracycline (OTC), norfloxacin (NFX), ciprofloxacin (CIP), and enrofloxacin (ENX) as non-structural analogues. Sensitivity analysis for SMX was performed over a concentration range of 100–4200 nmol·L^{-1}, with LOD calculated according to $3\sigma/k$ (where σ is the standard deviation of signals obtained from 10 blank sample measurements, and k is the slope of the calibration curve). Repeatability was validated through six replicate experiments. In actual sample testing, acetonitrile is added to milk and honey samples to precipitate the proteins. The supernatant was then co-injected with the material into the microfluidic chip for adsorption and detection. All results were validated against HPLC measurements.

3 Results and discussion

3.1 Characterization

The synthesis of Fe_3O_4@PCN-222@MIP commenced with the dark self-assembly of the template molecule SMX with functional monomers 4-VP and MAA in a methanol medium, followed by *in-situ* growth on the Fe_3O_4@PCN-222 surface (Schemes 1(a) and 1(b)). The selection of functional monomers is crucial for achieving superior recognition performance. A comparison of the performance of 4-VA, AM, 4-VP, and MAA, and the mixed monomer (4-VP:MAA), revealed that the mixed monomer provides more diverse recognition sites, resulting in the best recognition effect (Fig. S2(a) in the ESM). Further optimization indicated that the optimal molar ratios for SMX with functional monomers were SMX:4-VP:MAA = 1:2:2 (Fig. S2(c) in the ESM), and with the crosslinker were SMX: EDGMA = 1:10 (Fig. S2(d) in the ESM). Thus, the final optimal synthesis conditions were determined as SMX:4-VP:MAA:EDGMA = 1:2:2:10, yielding an IF of 1.73 (Table S1 in the ESM).

SEM images (Figs. 1(a) and 1(b)) show that Fe_3O_4 exhibits a cubic structure, and Fe_3O_4@PCN-222@MIP clearly reveals cubic Fe_3O_4 [43], rod-shaped PCN-222 [44], and small MIP particles. TEM images (Fig. 1(c)) reveal that Fe_3O_4@PCN-222@MIP exhibits a distinct core–shell structure, comprising a dark PCN-222 core, a gray Fe_3O_4 layer on the surface, and a thin, gauze-like MIP shell [45]. The XRD patterns of Fe_3O_4 and PCN-222 (Fig. 1(d)) are consistent with previously reported patterns, confirming their successful synthesis. The diffraction peaks of Fe_3O_4@PCN-222 include the characteristic peaks of Fe_3O_4 [46] and PCN-222 [47]. After MIP coating, the PCN-222-specific peak positions in the diffraction pattern of Fe_3O_4@PCN-222@MIP disappear. This occurs because the thick amorphous molecularly imprinted polymer coating significantly attenuates the diffraction signal from the underlying crystalline metal-organic framework. This phenomenon is commonly observed and widely recognized in previously reported MOF@MIP composites [48, 49]. The characteristic peak at 590 cm^{-1} in the FT-IR spectrum (Fig. 1(e)) originates from the Fe-O bond in Fe_3O_4. The strong peak at 3500–3200 cm^{-1} in Fe_3O_4@PCN-222@MIP is caused by the –OH stretching vibration in PCN-222, while the strong peak at 770 cm^{-1} is attributed to the Zr–O stretching vibration, confirming the successful composite formation of Fe_3O_4, PCN-222, and MIP. The VSM spectrum (Fig. 1(f)) shows that the saturation magnetization of Fe_3O_4 is 78.36 emu·g^{-1}. After composite with PCN-222, the saturation magnetization of Fe_3O_4@PCN-222 decreases to 30–40 emu·g^{-1}. After encapsulation with MIP, the magnetic susceptibility of Fe_3O_4@PCN-222@MIP is slightly lower than that of Fe_3O_4@PCN-222. Fe_3O_4@PCN-222@MIP exhibits a Type IV adsorption–desorption isotherm with a hysteresis loop (Fig. S3(a) in the ESM), indicating that Fe_3O_4@PCN-222@MIP possesses a mesoporous structure. The Brunauer–Emmett–Teller (BET) pore size of Fe_3O_4@PCN-222@MIP (Fig. S3(b) in the ESM) is 4 nm, confirming the abundant mesoporous structure of Fe_3O_4@PCN-222@MIP, which facilitates the exposure of adsorption active sites

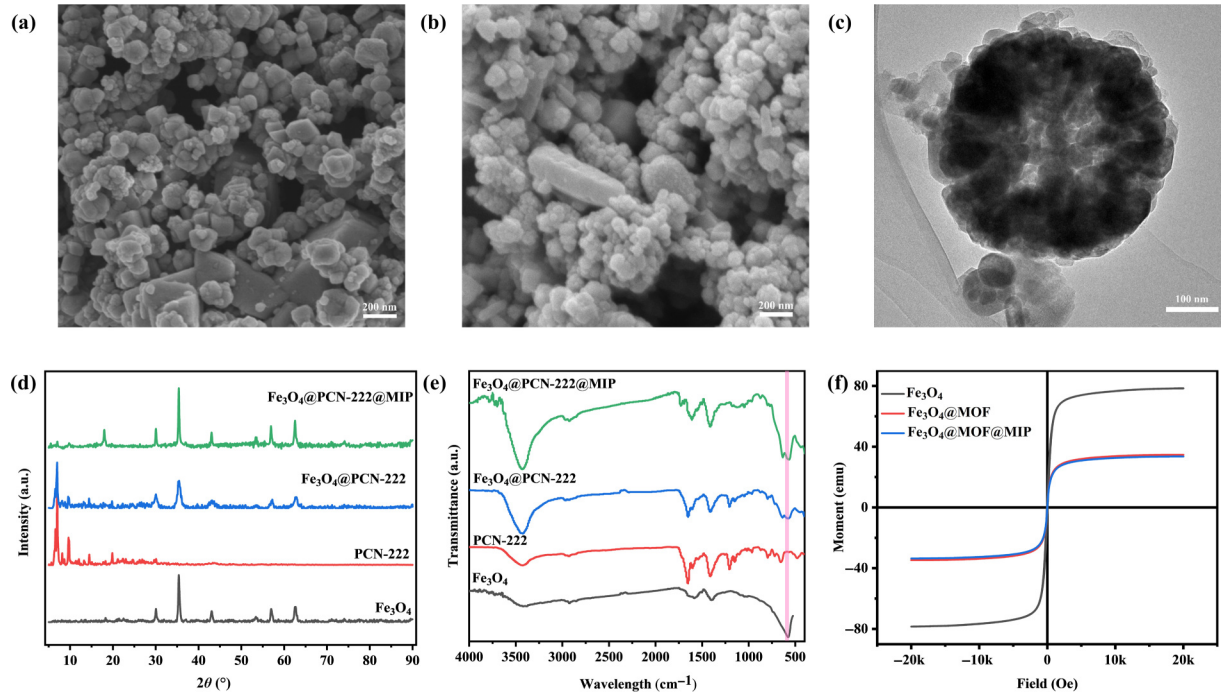

Figure 1 Characterization of nanomaterials. (a) SEM image of Fe_3O_4. (b) SEM image of Fe_3O_4@PCN-222@MIP. (c) TEM image of Fe_3O_4@PCN-222@MIP. (d) XRD patterns of Fe_3O_4@PCN-222@MIP. (e) FT-IR spectra of Fe_3O_4@PCN-222@MIP. (f) VSM patterns of Fe_3O_4@PCN-222@MIP.

and promotes the adsorption of SMX. The TG spectrum (Fig. S3(c) in the ESM) shows that Fe_3O_4@PCN-222@MIP exhibits two significant weight losses at 439 and 800 °C, respectively, corresponding to the decomposition of the surface MIP and the evaporation of residual solvents, as well as the destruction of the PCN-222 crystal structure. According to the XPS spectra of Fe_3O_4@PCN-222@MIP (Figs. S3(d)–S3(f) in the ESM), significant signals of Fe, Zr, O, C, and N were detected, indicating that Fe_3O_4@PCN-222@MIP was successfully synthesized [50].

3.2 Fe_3O_4@PCN-222@MIP recognition mechanism of SMX

Based on density functional theory (DFT), the geometric structures of the template molecule SMX and the functional monomer molecules 4-VP and MAA were investigated (Figs. 2(a)–2(c)), and the binding modes and binding energies between SMX and 4-VP and MAA were calculated. Figure 2(d) presents a color-coded schematic illustrating the relationship between types of intermolecular interactions and associated physical quantities, such as the second hyperpolarizability λ_2, the sign of the electron correlation effect ρ, and others. The blue region indicates strong attractive interactions, the green region corresponds to van der Waals interactions, and the red region represents strong repulsive interactions, commonly observed in steric effects of ring/cage structures. The blue isosurfaces in NCI represent hydrogen bonds (Fig. 2(e)), specifically the N–H···O hydrogen bonds formed between the carbon–oxygen double bond of the carboxyl group in the MAA molecule and the N–H group of the imino group in the SMX molecule, as well as the O–H···O hydrogen bonds. Large green isosurfaces appear between the aromatic rings of the SMX molecule and the 4-VP molecule, indicating the presence of π–π stacking between the two aromatic rings. Therefore, the interactions between the three molecules SMX, 4-VP, and MAA are primarily constituted by hydrogen bonds and π–π stacking (Fig. 2(f)).

To investigate the recognition process of SMX and the MIP cavity, we moved the SMX molecules along a direction perpendicular to the cavity plane by 0.5, 1.0, 1.5, 2.0, and 2.5 nm (corresponding to 5, 10, 15, 20, and 25 Å), respectively, to simulate their dynamic recognition process. Snapshots of the equilibrium trajectories are shown in Fig. S4(a) in the ESM. Analysis of displacement changes (Fig. S4(b) in the ESM) indicates that when the initial displacement is 0.3 nm, SMX remains stable near 0.3 nm throughout the entire kinetic process, indicating that this distance is the most stable; when the initial displacement is 0.2 nm, SMX ultimately stabilizes at approximately 0.3 nm. When the initial displacement is greater than or equal to 0.4 nm, SMX further moves outward and ultimately equilibrates at approximately 0.6 nm. When placed at an initial displacement of 0.1 nm, the SMX molecule experiences a strong repulsive force from the cavity. As a result, it moves outward beyond the local stable point at 0.3 nm and ultimately equilibrates at approximately 0.5 nm. In summary, the cavity exerts a repulsive force on SMX, whose strength varies with the initial distance: it is maximum at 0.1 nm, weakens to a minimum at 0.2–0.3 nm, and remains essentially stable and weaker than at 0.2 nm at 0.4–0.5 nm. System equilibrium and structural stability (root mean square deviation (RMSD), Fig. S4(c) in the ESM) show that, except for the system with an initial displacement of 0.1 nm, which eventually stabilizes at 0.4 nm, all others stabilize at approximately 0.2 nm, indicating equilibrium. The system with an initial displacement of 0.5 nm (5 Å displacement) exhibits the smallest RMSD fluctuations and the most stable structure (consistent with the shorter displacement distance). The initial RMSD of the system with an initial displacement of 0.3 nm (3 Å displacement) was relatively high, but stabilized at 0.2 nm after 5 ns, indicating that the conformation tended to stabilize. The RMSD results were consistent with the displacement analysis: SMX was most stable at 0.3 nm (both displacement and RMSD were minimal). When the initial displacement is 0.4 to 0.5 nm, SMX first moves outward and then stabilizes; when the initial displacement is

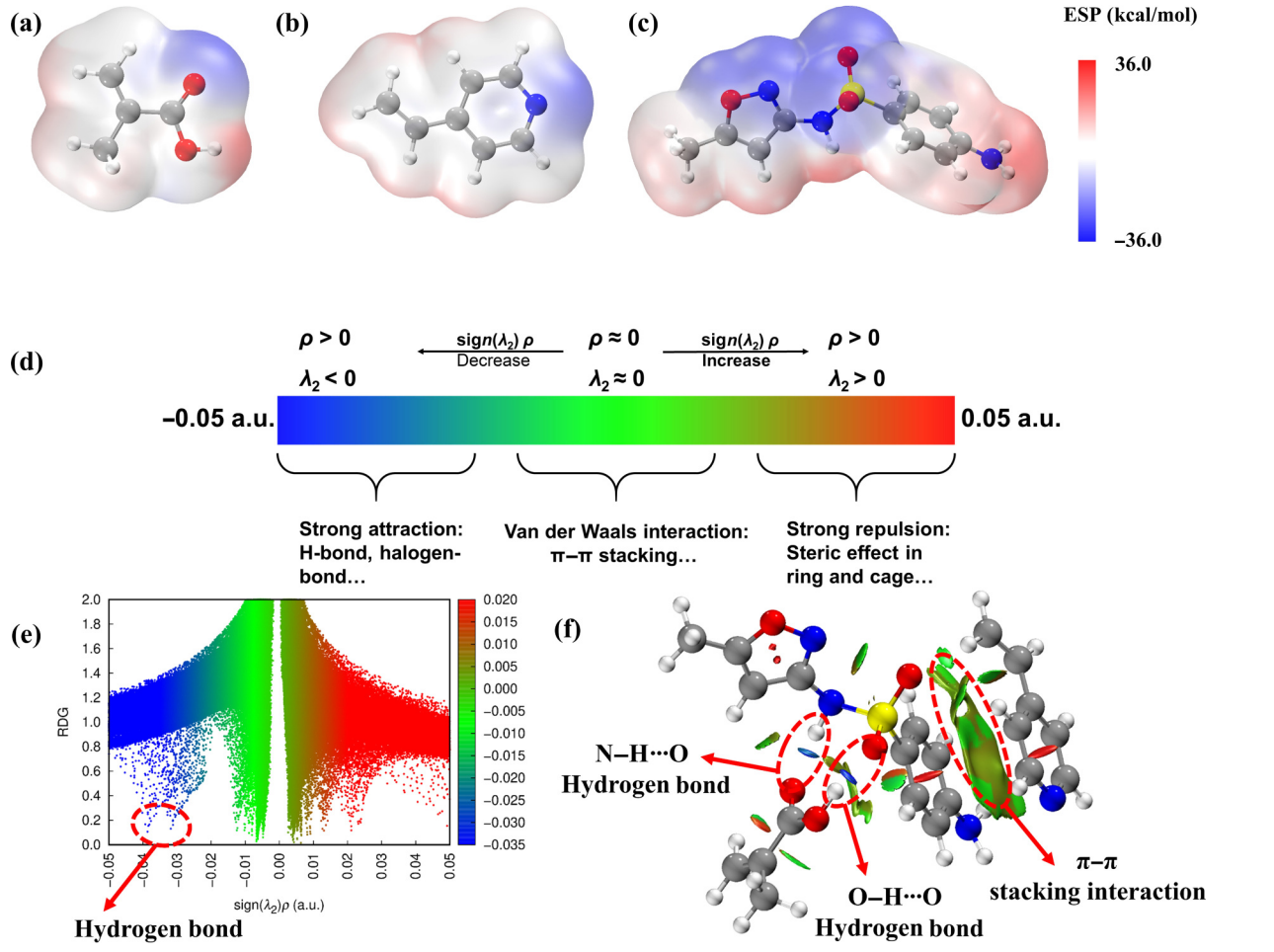

Figure 2 MIP identification SMX theoretical calculation. (a) Structural formula of MAA. (b) Structural formula of 4-VP. (c) Structural formula of SMX. (d) Equipotential surface distribution. (e) Hydrogen bonding positions in isopotential surfaces. (f) Structure of SMX after combination with MAA and 4-VP.

0.1 nm, the RMSD continues to increase, indicating that SMX rapidly moves away from the cavity center. Interaction energy analysis (Fig. S4(d) in the ESM) shows that the interaction energy decreases as the distance between SMX and the cavity center increases. At an initial displacement of 0.1 nm, the interaction energy continues to decrease, confirming that SMX is moving away from the cavity (consistent with Figs. S4(b) and S4(c) in the ESM). At other displacements, the interaction energy remains largely stable, indicating no significant relative displacement between SMX and the cavity.

3.3 Weakening the catalytic mechanism of Fe_3O_4@PCN-222@MIP-SMX

To further investigate its enzymatic kinetic properties, we determined the corresponding apparent steady-state kinetic parameters. Based on Lineweaver–Burk plots and typical Michaelis–Menten equation fitting results (Fig. S5 in the ESM), the apparent Michaelis–Menten constants (K_m) of Fe_3O_4@PCN-222@MIP for TMB and H_2O_2 were determined to be 0.057 mM and 0.719 mM, respectively (Table S4 in the ESM). These results indicate that the material exhibits high catalytic affinity for both substrates. Such outstanding catalytic performance may originate from the abundant active iron centers on the surface of Fe_3O_4@PCN-222@MIP.

Compared to Fe_3O_4@PCN-222@MIP, the high-resolution scan C 1s values of Fe_3O_4@PCN-222@MIP-SMX show a negative shift, indicating the formation of π–π stacking and hydrogen bonding interactions between Fe_3O_4@PCN-222@MIP and SMX (Fig. 3(a)). Upon combination with Fe_3O_4@PCN-222@MIP, SMX can attenuate the peroxidase-like activity of Fe_3O_4@PCN-222@MIP through electronic interactions. Compared to Fe_3O_4@PCN-222@MIP, the FT-IR spectrum of Fe_3O_4@PCN-222@MIP-SMX exhibits an absorption peak at 1710 cm^{-1}, which is attributed to the binding of SMX to Fe_3O_4@PCN-222@MIP (Fig. 3(b)). Compared to Fe_3O_4@PCN-222@MIP, the high-resolution scanning Fe 2p value (711.83 eV) of Fe_3O_4@PCN-222@MIP-SMX shifted negatively by 0.80 eV (Fig. 3(c)), This is due to the transfer of electrons from Fe to S after Fe_3O_4@PCN-222@MIP adsorbs SMX. Comparing the high-resolution scanning S 2p values of SMX and Fe_3O_4@PCN-222@MIP-SMX (Fig. 3(d)), a significant positive shift is observed, confirming that electrons have transferred from Fe to S, thereby weakening the Fenton reaction of Fe_3O_4@PCN-222@MIP. Compared to Fe_3O_4@PCN-222@MIP, the Fe_3O_4@PCN-222@MIP-SMX composite exhibits weaker EPR activity (Fig. 3(e)), suggesting that after Fe_3O_4@PCN-222@MIP binds with SMX, electrons transfer to S, inhibiting the peroxidase-like activity of Fe_3O_4@PCN-222@MIP and reducing ·OH generation. These results indicate that the electronic interaction between SMX and Fe_3O_4@PCN-222@MIP inhibits the enzyme-like activity of Fe_3O_4@PCN-222@MIP. As expected, upon addition of SMX, Fe_3O_4@PCN-

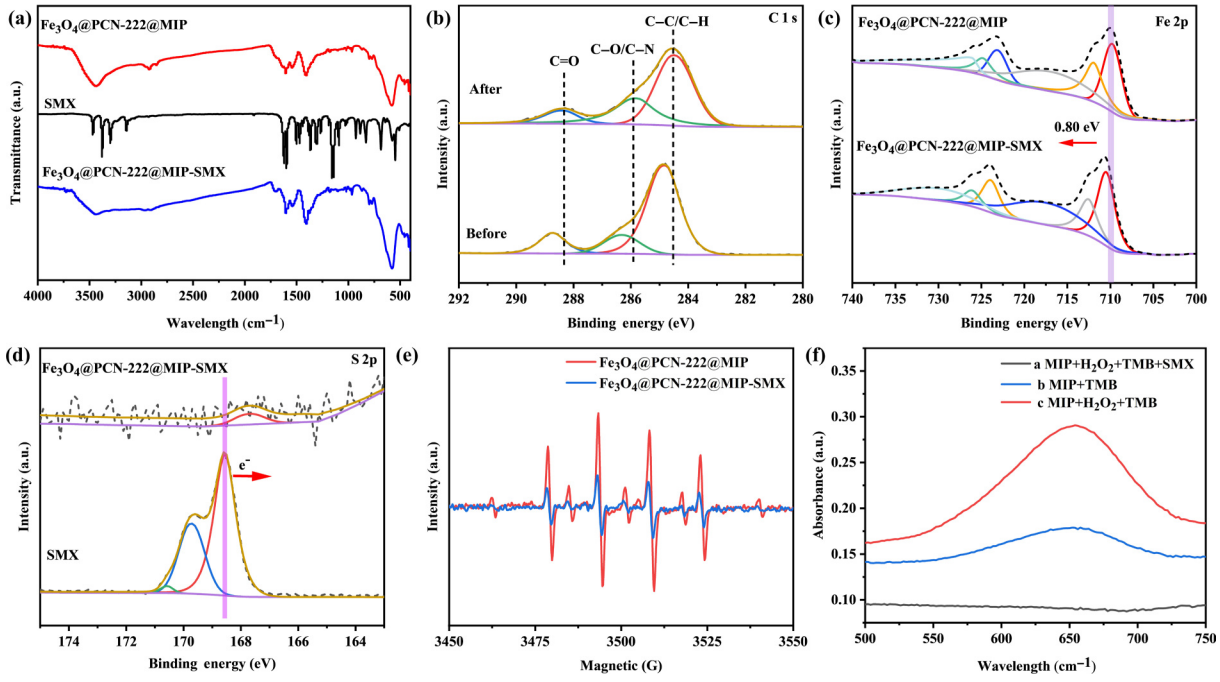

Figure 3 Colorimetric detection mechanism. (a) FT-IR spectra: Fe_3O_4@PCN-222@MIP, SMX, and Fe_3O_4@PCN-222@MIP-SMX. (b) High-resolution XPS spectra: C 1s of Fe_3O_4@PCN-222@MIP and Fe_3O_4@PCN-222@MIP-SMX spectra. (c) High-resolution XPS spectra: Fe 2p spectra of Fe_3O_4@PCN-222@MIP and Fe_3O_4@PCN-222@MIP-SMX. (d) High-resolution XPS spectra: S 2p spectra of SMX and Fe_3O_4@PCN-222@MIP-SMX. (e) EPR spectra: Fe_3O_4@PCN-222@MIP (red curves) and Fe_3O_4@PCN-222@MIP-SMX (blue curve). (f) Ultraviolet–visible (UV–Vis) absorption spectra of different reaction systems and the associated color changes (inset).

222@MIP reduces the oxidation of TMB through complexation with SMX, thereby lowering the absorbance (Fig. 3(f)). Therefore, the colorimetric sensor based on Fe_3O_4@PCN-222@MIP can be used for the detection of SMX. To validate the specificity of the MIP, we compared the responses of Fe_3O_4@PCN-222@MIP and Fe_3O_4@PCN-222@NIP under identical conditions (Fig. S6 in the ESM). Under 4200 nmol·L^{-1} SMX exposure, the MIP exhibited a signal change rate of 115.08% ± 3.21%, whereas the NIP showed only 28.46% ± 3.25%. This confirms that the signal variation primarily stems from specific binding within the imprinted cavity rather than non-specific interactions.

3.4 Adsorption kinetics study and adsorption isotherm study

Adsorption kinetics fitting and adsorption isotherm fitting are important tools for determining the adsorption mechanism and adsorption performance of adsorbents. The results of adsorption kinetics fitting are shown in the supplementary information (Fig. S7(a) in the ESM). Adsorption kinetics fitting shows that during the initial adsorption phase, the adsorption capacity of SMX increases with prolonged adsorption time. When the adsorption time approaches 100 min, the adsorption capacity tends toward saturation. Table S2 in the ESM) lists the simulation parameters for the two kinetic models applied to the SMX adsorption data. The results indicate that the correlation coefficients R^2 values (0.7027–0.9583) for the pseudo-first-order kinetic model (Fig. S7(b) in the ESM) were significantly lower than those for the pseudo-second-order kinetic model (Fig. S7(c) in the ESM) (0.9903–0.99973), suggesting that the pseudo-second-order kinetic model is more suitable for explaining the adsorption behavior of SMX on Fe_3O_4@PCN-222@MIP.These results further indicate that the adsorption process is primarily chemical adsorption. Molecular dynamics simulations indicate that SMX can reach a stable equilibrium position (approximately 0.3 nm) within the cavity, driven by hydrogen bonding and π–π stacking interactions. This rapid formation of a stable complex at the molecular level aligns with the fast initial adsorption observed in kinetic experiments and supports the pseudo-second-order kinetic model based on the assumption that chemical adsorption is the rate-limiting step [51].

The fitting results of the adsorption isotherms are shown in the supplementary information (Fig. S7(d) in the ESM). The adsorption processes at 298 K were studied using the Langmuir (Fig. S7(e) in the ESM) and Freundlich (Fig. S7(f) in the ESM) adsorption isotherm models. The linear fitting results of the Langmuir adsorption model and the Freundlich adsorption model, along with the simulation parameters for the SMX adsorption data using both isotherm models, are listed in (Table S3 in the ESM). The linear correlation coefficient R^2 (0.9097–0.9251) of the Freundlich adsorption model is greater than that of the Langmuir adsorption model (0.6797–0.8081), indicating that the thermodynamic adsorption of SMX on Fe_3O_4@PCN-222@MIP is multi-layer adsorption.

3.5 Fe_3O_4@PCN-222@MIP for colorimetric detection of SMX

To achieve efficient analysis and detection of SMX using Fe_3O_4@PCN-222@MIP, key parameters of the MSPE process were systematically optimized. The amount of adsorbent and sample loading flow rate were identified as critical factors affecting extraction efficiency. A dosage of 8 mg of Fe_3O_4@PCN-222@MIP was selected to balance enrichment factor and processing time, while a flow rate of 10 μL·min^{-1} was optimal to ensure high adsorption efficiency and prevent material leakage (Figs. S8(a) and S8(b) in the ESM). After five cycles, the material retained over 80% of its adsorption capacity (Fig. S8(c) in the ESM). Furthermore, the colorimetric detection conditions were thoroughly investigated. The

optimal concentrations of Fe_3O_4@PCN-222@MIP, H_2O_2, and TMB were determined to be 8 mg, 5 mmol·L^{-1}, and 0.7 μmol·L^{-1}, respectively. The reaction performed best at pH 3.5, room temperature, and within 20 min (Figs. S8(d)–S8(i) in the ESM). To evaluate the integrated performance of the chip, we compared direct colorimetry with magnetic solid-phase extraction-colorimetry on the chip (Fig. S9 in the ESM). Results demonstrated that the chip achieved an extraction efficiency of 95.45% ± 5.70% for SMX, with detection signals comparable to direct colorimetry. This confirms the platform's capability for integrated operation of efficient extraction and *in-situ* detection.

The detection performance of the strategy for SMX was evaluated under optimal conditions. The color change of Fe_3O_4@PCN-222@MIP was also investigated under different SMX concentrations, which could be recorded by a smartphone rather than a microplate reader, and a cassette tape with a white LED was used to eliminate environmental interference. Based on the color changes, the relationship between gray scale values and SMX concentration was determined and obeyed a regression equation of $y = 13.77x + 98.21$ with an R^2 of 0.9725 (Fig. 4(a)). The LOD calculated based on $3\sigma/k$ [52] was 632.74 nmol·L^{-1}. The separation efficiency of the method for SMX was verified by the color change (Fig. 4(b)), which showed that only the color of antibiotics in the class of SDs was weakened, and the color of other substances was enhanced, which proved that the method had a good identification efficiency for antibiotics in the class of SDs. The relative standard deviation (RSD) of the method was 3.28% for six tests (Fig. 4(c)), which showed good reproducibility. The results indicated that the Fe_3O_4@PCN-222@MIP prepared in this study had good detection performance for SMX. Unlike signal enhancement strategies relying on precision optical waveguides or AIE nanofibers, this study integrates multifunctional materials with microfluidics to enable rapid point-of-care screening without complex instrumentation [53].

3.6 Analysis of real samples

To further validate the reliability of this method in real sample analysis, SMX was detected in milk and honey. Sample pretreatment was performed according to the method described in Section 2.6, and recovery experiments were conducted to assess the applicability of this method in real samples (Fig. 4(d)). The results are shown in Table 1, with recovery rates for spiked samples ranging from 94.4% to 103.7% (milk) and 91.5% to 102.9% (honey). In this work, HPLC as a commonly used method, was compared with a colorimetric sensor, yielding recovery rates of 98.6%–107.5%. Compared with HPLC detection and methods reported in the literature; this method exhibits satisfactory analytical performance (Table S5 in the ESM). These results indicate that the method has good reliability and is suitable for the detection of SMX in milk and honey.

4 Conclusions

In this work, successfully synthesized the multifunctional composite

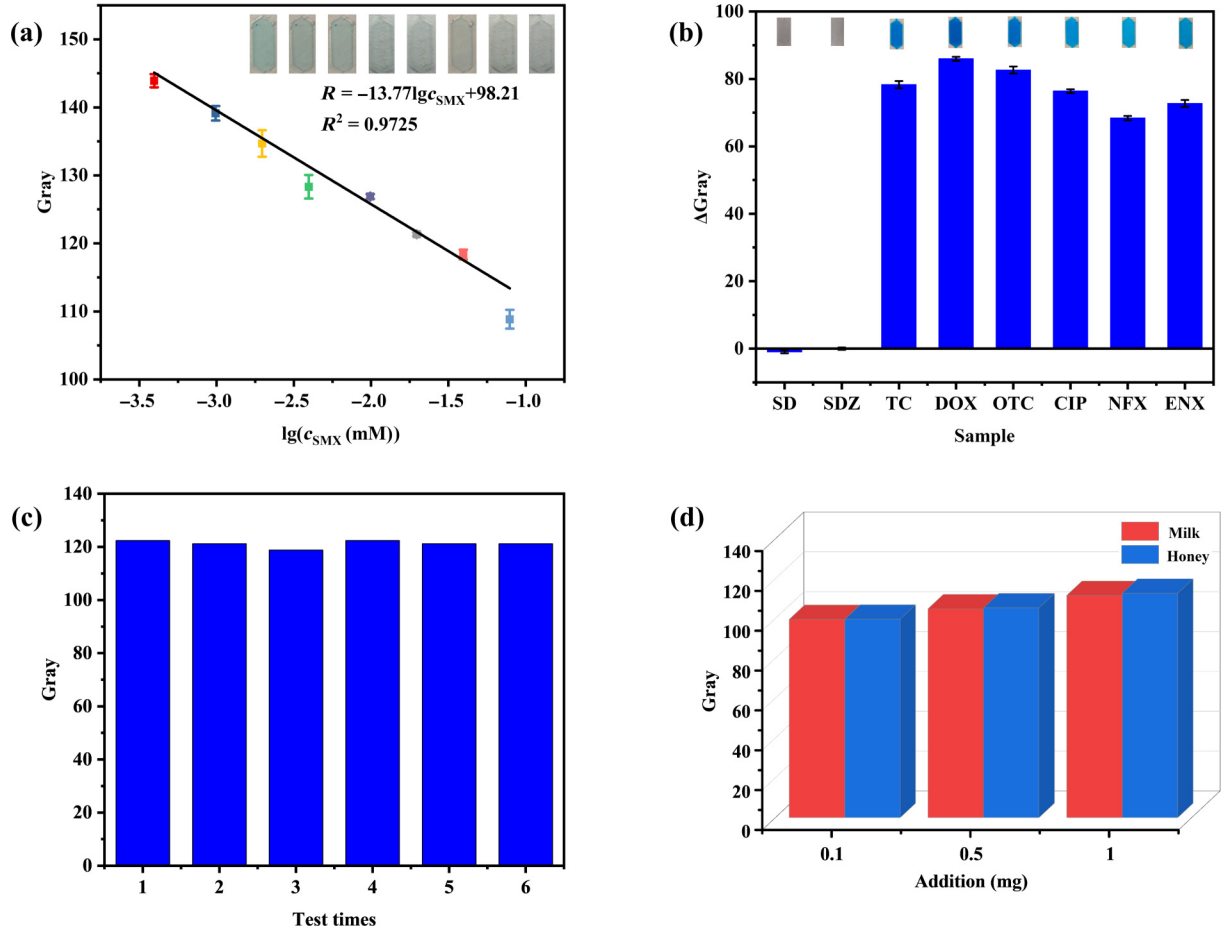

Figure 4 Analytical performance of on-chip MIP-MSPE-colorimetry. (a) Sensitivity of on-chip MIP-MSPE-colorimetry. (b) Specificity of on-chip MIP-MSPE-colorimetry. (c) Reproducibility of on-chip MIP-MSPE colorimetry. (d) Actual sample testing.

Table 1 Analytical results for the determination of SMX in real samples by colorimetric detection method ($n = 3$)

Samples	Addition (mg)	Detectable amount (mg)	RSD (%)	Recoveries (%)
Milk	0.10	0.097 ± 0.004	5.2	94.4
	0.50	0.483 ± 0.036	7.9	103.7
	1.00	0.972 ± 0.058	4.2	97.1
Honey	0.10	0.104 ± 0.002	8.3	91.5
	0.50	0.517 ± 0.079	6.7	102.9
	1.00	1.05 ± 0.051	4.9	101.1

material Fe_3O_4@PCN-222@MIP by integrating magnetic Fe_3O_4 nanoparticles, zirconium-based metal-organic frameworks (PCN-222), and molecularly imprinted polymers. The total synthesis time for this material is approximately 55 h, with an overall yield of about 85%. This material synergistically combines the high specific surface area and stability of metal-organic frameworks, the magnetic response properties of Fe_3O_4 (facilitating separation), and the specific recognition capability of the molecularly imprinted layer for SMX. DFT calculations indicate that specific recognition of SMX is primarily achieved through hydrogen bonding and π–π stacking interactions within the imprinted cavities, whose shape, size, and functional groups complement the template molecule. Furthermore, the inherent POD-like activity of this material (primarily attributed to the Fe_3O_4 component) enables direct colorimetric detection upon target binding. This process establishes a chip-based MSPE colorimetric assay through electron transfer between the material and SMX. This method enables highly selective, sensitive (LOD = 632.74 nmol·L^{-1}) integrated separation, enrichment, and detection of SMX. Satisfactory recovery rates were achieved in complex food samples (milk and honey), validating its practicality and reliability. Compared to existing methods (Table S5 in the ESM), this strategy employs a microfluidic platform to achieve a simplified, elution-free workflow. While certain methods offer lower detection limits, the core breakthrough of this study lies in eliminating the elution step and truly integrating identification, extraction, and detection into a single, seamless microfluidic workflow, thereby enabling simpler and faster analysis. This system demonstrates broad adaptability. By replacing the template molecule and selecting MOFs with matching pore sizes, it can be extended to analyze other target substances. This work not only provides a viable approach for efficient trace antibiotic monitoring but also reveals universal design principles for smart MOF composites applicable to environmental sensing and analytical applications.

Electronic Supplementary Material: Supplementary Material (schematic and physical diagrams of the microfluidic chip; optimization of MIP synthesis conditions; material characterization; theoretical calculations for SMX recognition by MIP; catalytic kinetic characterization; selectivity comparison between MIP and NIP; adsorption kinetics and isotherm fitting; optimization of on-chip MSPE-colorimetric detection conditions; chip performance evaluation; imprinting factor; adsorption kinetics and isotherm fitting parameters; comparison of Michaelis–Menten constants; and comparison with other detection methods) is available in the online version of this article at https://doi.org/10.26599/NR.2026.94908495.

Data availability

All data needed to support the conclusions in the paper are presented in the manuscript and the Electronic Supplementary Material. Additional data related to this paper may be requested from the corresponding author upon request.

Acknowledgements

This work was supported by the National Key R&D Program of China (No. 2022YFC3400700).

Declaration of competing interest

All the contributing authors report no conflict of interests in this work.

Author contribution statement

Z. Y. Z.: Conceptual design, methodology, validation, formal analysis, and initial draft preparation. G. W. X., L. X., and J. W. L.: Manuscript organization, formal analysis, and software development. W. T. Y., W. Q. H., and Z. R. W.: Resource preparation, methodology, and investigative research. Z. H. L.: Methodology. J.-M. L.: Writing – review & editing, project management, and funding acquisition. All authors approved the final manuscript.

Use of AI statement

None.

References

[1] Wang, R. M.; Ji, M.; Zhai, H. Y.; Guo, Y. J.; Liu, Y. Occurrence of antibiotics and antibiotic resistance genes in WWTP effluent-receiving water bodies and reclaimed wastewater treatment plants. *Sci. Total Environ.* **2021**, *796*, 148919.

[2] Lyu, J.; Yang, L. S.; Zhang, L.; Ye, B. X.; Wang, L. Antibiotics in soil and water in China-a systematic review and source analysis. *Environ. Pollut.* **2020**, *266*, 115147.

[3] Zhou, Z. Y.; Gong, X. X.; Yu, C. L.; Lai, L.; Ding, L. W.; Hu, Y.; Yang, Y. Y.; Zeng, C. H. On-site visual sensing of antibiotics in food by new fluorescent lanthanide metal-organic frameworks. *Microchem. J.* **2024**, *206*, 111651.

[4] Limbu, S. M.; Chen, L. Q.; Zhang, M. L.; Du, Z. Y. A global analysis on the systemic effects of antibiotics in cultured fish and their potential human health risk: A review. *Rev. Aquac.* **2021**, *13*, 1015–1059.

[5] Prasannamedha, G.; Kumar, P. S. A review on contamination and removal of sulfamethoxazole from aqueous solution using cleaner techniques: Present and future perspective. *J. Clean. Prod.* **2020**, *250*, 119553.

[6] Thiebault, T. Sulfamethoxazole/trimethoprim ratio as a new marker in raw wastewaters: A critical review. *Sci. Total Environ.* **2020**, *715*, 136916.

[7] Iftikhar, N.; Zafar, R.; Hashmi, I. Multi-biomarkers approach to determine the toxicological impacts of sulfamethoxazole antibiotic on freshwater fish *Cyprinus carpio*. *Ecotoxicol. Environ. Saf.* **2022**, *233*, 113331.

[8] Bajkacz, S.; Felis, E.; Kycia-Słocka, E.; Harnisz, M.; Korzeniewska, E. Development of a new SLE-SPE-HPLC-MS/MS method for the determination of selected antibiotics and their transformation products in anthropogenically altered solid environmental matrices. *Sci. Total Environ.* **2020**, *726*, 138071.

[9] Oshaghi, S. Nano-sized magnetic molecularly imprinted polymer solid-phase microextraction for highly selective recognition and enrichment of sulfamethoxazole from spiked water samples. *J. Chromatogr. A* **2024**, *1729*, 465016.

[10] Lee, G.; Lee, S.; Oh, S.; Kim, D.; Oh, M. Tip-to-middle anisotropic MOF-On-MOF growth with a structural adjustment. *J. Am. Chem. Soc.* **2020**, *142*, 3042–3049.

[11] Wu, X. Y.; Gao, Y. X.; Bi, J. H. Understanding the structure-dependent adsorption behavior of four zirconium-based porphyrinic MOFs for the removal of pharmaceuticals. *Microporous Mesoporous Mater.* **2024**, *363*, 112827.

[12] Huang, H. Z.; Wang, H. F.; Du, K. Y.; Yu, X. P.; Shentu, X. P. Bi-model detection of sulfonamide antibiotics using a microfluidic chip-lateral flow immunoassay based on liposome-modified PCN-222. *Biosens. Bioelectron.* **2025**, *279*, 117393.

[13] Wu, L. H.; Luo, Y.; Wang, C. F.; Wu, S. L.; Zheng, Y. F.; Li, Z. Y.; Cui, Z. D.; Liang, Y. Q.; Zhu, S. L.; Shen, J. et al. Self-driven electron transfer biomimetic enzymatic catalysis of bismuth-doped PCN-222 MOF for rapid therapy of bacteria-infected wounds. *ACS Nano* **2023**, *17*, 1448–1463.

[14] Tian, X.; Gao, Y. M.; Lou, X. J.; Zhu, J. W.; Qin, M. J.; Lu, M. H. Construction of PCN-222@PCN-134 as sorbent of dispersive solid-phase extraction for extraction and enrichment of sulphonamides. *Sep. Purif. Technol.* **2024**, *342*, 127055.

[15] Xu, C.; He, M.; Chen, B. B.; Hu, B. Magnetic porous coordination networks for preconcentration of various metal ions from environmental water followed by inductively coupled plasma mass spectrometry detection. *Talanta* **2022**, *245*, 123470.

[16] He, S. N.; Zhang, L. P.; Bai, S. K.; Yang, H.; Cui, Z.; Zhang, X. F.; Li, Y. P. Advances of molecularly imprinted polymers (MIP) and the application in drug delivery. *Eur. Polym. J.* **2021**, *143*, 110179.

[17] Ali, G. K.; Omer, K. M. Molecular imprinted polymer combined with aptamer (MIP-aptamer) as a hybrid dual recognition element for bio(chemical) sensing applications. *Review. Talanta* **2022**, *236*, 122878.

[18] Bakhshizadeh, S.; Ghaedi, M.; Dashtian, K.; Sabzehmeidani, M. M.; Abbasi-Asl, H. Molecularly imprinted polymer based on MIL-101 (Cr) MOF incorporated polyvinylidene for selective adsorption and separation dye with improved antifouling properties. *Colloids Surf. A: Physicochem. Eng. Asp.* **2024**, *702*, 134545.

[19] Jiang, P.; Niu, Y. L.; Cao, J. P.; Xie, D.; Li, J. Q.; Guo, T. Y. A MOF-doped molecularly imprinted polymer/MOF hybrid gel incorporating with pH-buffering sodium acrylate for practical detoxification of organophosphorus nerve agents. *Chem. Eng. J.* **2024**, *481*, 148377.

[20] Li, H.; Wang, D. H.; Liu, W.; Ma, Z.; Wang, D. N.; Li, Y.; Huan, W. W.; Zhang, Y. M. A LMOF/MIP paper-based chip and analysis of tetracycline in foodstuff with sample-to-answer performance. *Talanta* **2025**, *281*, 126879.

[21] Kardani, F.; Mirzajani, R.; Tamsilian, Y.; Kiasat, A.; Bakhshandeh Farajpour, F. A novel immunoaffinity column based metal-organic framework deep eutectic solvents @ molecularly imprinted polymers as a sorbent for the solid phase extraction of aflatoxins AFB1, AFB2, AFG1 and AFG2 from cereals samples. *Microchem. J.* **2023**, *187*, 108366.

[22] Geng, L. J.; Huang, J. C.; Fang, M. X.; Wang, H. F.; Liu, J. J.; Wang, G. X.; Hu, M. J.; Sun, J. S.; Guo, Y. M.; Sun, X. Recent progress of the research of metal-organic frameworks-molecularly imprinted polymers (MOFs-MIPs) in food safety detection field. *Food Chem.* **2024**, *458*, 140330.

[23] Yang, X. G.; Xu, L. P.; Xiong, S. J.; Rao, H.; Tan, F. C.; Yan, J. H.; Bao, Y. J.; Albanese, A.; Camposeo, A.; Pisignano, D. et al. Light-emitting microfibers from lotus root for eco-friendly optical waveguides and biosensing. *Nano Lett.* **2024**, *24*, 566–575.

[24] Chen, Z.; Zhang, Z. Y.; Qi, J.; You, J. M.; Ma, J. P.; Chen, L. X. Colorimetric detection of heavy metal ions with various chromogenic materials: Strategies and applications. *J. Hazard. Mater.* **2023**, *441*, 129889.

[25] Li, F.; Jiang, J. M.; Shen, N. T.; Peng, H.; Luo, Y.; Li, N. N.; Huang, L. Y.; Lu, Y. Y.; Liu, L. F.; Li, B. et al. Flexible microfluidic colorimetric detection chip integrated with $ABTS^{\cdot+}$ and $Co@MnO_2$ nanozyme catalyzed TMB reaction systems for bio-enzyme free detection of sweat uric acid. *Anal. Chim. Acta* **2024**, *1299*, 342453.

[26] Wu, S. W.; Guo, D. Z.; Xu, X. C.; Pan, J. M.; Niu, X. H. Colorimetric quantification and discrimination of phenolic pollutants based on peroxidase-like Fe_3O_4 nanoparticles. *Sens. Actuators B: Chem.* **2020**, *303*, 127225.

[27] Liu, C.; Zhao, X. P.; Wang, Z. C.; Zhao, Y. Y.; Li, R. F.; Chen, X. Y.; Chen, H.; Wan, M. N.; Wang, X. Q. Metal-organic framework-modulated Fe_3O_4 composite au nanoparticles for antibacterial wound healing via synergistic peroxidase-like nanozymatic catalysis. *J. Nanobiotechnol.* **2023**, *21*, 427.

[28] Li, J. W.; Yin, Y. L.; Li, J. X.; Zhu, Z. Y.; Meng, F. F.; Liu, Y. K.; Wang, Z. R.; Liu, B.; Li, Z. H. II-type heterojunction of $FeTiO_3$@PCN-223(Zn) with oxygen vacancies established by ball milling for visible-light-driven photo-Fenton degradation of tetracycline hydrochloride. *Environ. Res.* **2025**, *285*, 122648.

[29] Mourdikoudis, S.; Dutta, S.; Kamal, S.; Gómez-Graña, S.; Pastoriza-Santos, I.; Wuttke, S.; Polavarapu, L. State-of-the-art, insights, and perspectives for MOFs-nanocomposites and MOF-derived (nano)materials. *Adv. Mater.* **2025**, *37*, 2415399.

[30] Garcia, S. M.; Wong, A.; Khan, S.; Sotomayor, M. D. P. T. A simple, sensitive and efficient electrochemical platform based on carbon paste electrode modified with Fe_3O_4@MIP and graphene oxide for folic acid determination in different matrices. *Talanta* **2021**, *229*, 122258.

[31] Sun, Y. K.; Ruan, S. L.; Zhou, Y. Y.; Zhao, L. H.; Xiong, W. J.; Lin, C. H.; Kuang, J. J.; Ning, F. H.; Zhang, M.; Zhang, H. Y. et al. A magnetic solid phase extraction microfluidic chip coupled with gas chromatography-mass spectrometry for the determination of polycyclic aromatic hydrocarbons in aqueous samples. *J. Chromatogr. A* **2023**, *1708*, 464364.

[32] Hariri, R.; Dehghanpour, S. Adsorptive removal and visible-light photocatalytic degradation of large cationic and anionic dyes induced by air-bubbles in the presence of a magnetic porphyrinic metal-organic framework (Fe_3O_4@SiO_2@PCN-222(Fe)). *J. Phys. Chem. Solids* **2021**, *155*, 110126.

[33] Li, J. X.; Liu, J. C.; Li, J. W.; Li, Y. P.; Zhu, Z. Y.; Wang, Z. R.; Yin, Y. L.; Li, Z. H. Construction of a Z-scheme PCN-222/$CoFe_2O_4$ heterojunction for efficient photo-Fenton tetracycline hydrochloride degradation: Mechanism and pathways. *J. Mater. Chem. A* **2025**, *13*, 31385–31394.

[34] Biswas, S.; Chen, Y. L.; Xie, Y.; Sun, X.; Wang, Y. Ultrasmall Au(0) inserted hollow PCN-222 MOF for the high-sensitive detection of estradiol. *Anal. Chem.* **2020**, *92*, 4566–4572.

[35] Han, X. F.; Zhang, X. H.; Zhong, L. J.; Yu, X.; Zhai, H. Y. Preparation of sulfamethoxazole molecularly imprinted polymers based on magnetic metal-organic frameworks/graphene oxide composites for the selective extraction of sulfonamides in food samples. *Microchem. J.* **2022**, *177*, 107259.

[36] Arabi, M.; Ostovan, A.; Li, J. H.; Wang, X. Y.; Zhang, Z. Y.; Choo, J.; Chen, L. X. Molecular imprinting: Green perspectives and strategies. *Adv. Mater.* **2021**, *33*, 2100543.
[37] Lamaoui, A.; Palacios-Santander, J. M.; Amine, A.; Cubillana-Aguilera, L. Fast microwave-assisted synthesis of magnetic molecularly imprinted polymer for sulfamethoxazole. *Talanta* **2021**, *232*, 122430.
[38] Zheng, C.; Xie, Y. C.; Niu, Y. X.; Wang, C. L.; Hu, J.; Kang, K.; Song, H.; Bai, S. P. Modeling of multi-temperature type I and II benzene/ammonia adsorption isotherms: Dual LF model and linearized DR model. *Sep. Purif. Technol.* **2024**, *338*, 126246.
[39] Vareda, J. P. On validity, physical meaning, mechanism insights and regression of adsorption kinetic models. *J. Mol. Liq.* **2023**, *376*, 121416.
[40] Zahra, S.; Zaib, S.; Khan, I. Identification of isobenzofuranone derivatives as promising antidiabetic agents: Synthesis, *in vitro* and *in vivo* inhibition of α-glucosidase and α-amylase, computational docking analysis and molecular dynamics simulations. *Int. J. Biol. Macromol.* **2024**, *259*, 129241.
[41] Wei, X.; Wei, Y. J.; Zhang, X.; Wu, C. X.; Chen, M. L.; Wang, J. H. A spiral microfluidic chip endows high efficiency single cell alignment at extremely low flow for ICP-MS analysis. *Microchem. J.* **2023**, *190*, 108635.
[42] Xing, G. W.; Shang, Y. T.; Wang, X. R.; Lin, H. F.; Chen, S. L.; Pu, Q. S.; Lin, L. Multiplexed detection of foodborne pathogens using one-pot CRISPR/Cas12a combined with recombinase aided amplification on a finger-actuated microfluidic biosensor. *Biosens. Bioelectron.* **2023**, *220*, 114885.
[43] Sahadevan, J.; Sojiya, R.; Padmanathan, N.; Kulathuraan, K.; Shalini, M. G.; Sivaprakash, P.; Esakki Muthu, S. Magnetic property of Fe_2O_3 and Fe_3O_4 nanoparticle prepared by solvothermal process. *Mater. Today Proc.* **2022**, *58*, 895–897.
[44] Zhang, Y.; Cao, X. G.; Liu, Y. C.; Zhao, Y. K.; Hou, X. H. Constructing BiOF@PCN-222 MOF heterojunction to remove tetracycline under visible light rapidly and efficiently. *J. Water Process Eng.* **2024**, *67*, 106184.
[45] Zeb, S.; Wong, A.; Khan, S.; Hussain, S.; Sotomayor, M. D. P. T. Using magnetic nanoparticles/MIP-based electrochemical sensor for quantification of tetracycline in milk samples. *J. Electroanal. Chem.* **2021**, *900*, 115713.
[46] Elshypany, R.; Selim, H.; Zakaria, K.; Moustafa, A. H.; Sadeek, S. A.; Sharaa, S. I.; Raynaud, P.; Nada, A. A. Elaboration of Fe_3O_4/ZnO nanocomposite with highly performance photocatalytic activity for degradation methylene blue under visible light irradiation. *Environ. Technol. Innov.* **2021**, *23*, 101710.
[47] Chang, P. H.; Mukhopadhyay, R.; Zhong, B.; Yang, Q. Y.; Zhou, S. G.; Tzou, Y. M.; Sarkar, B. Synthesis and characterization of PCN-222 metal organic framework and its application for removing perfluorooctane sulfonate from water. *J. Colloid Interface Sci.* **2023**, *636*, 459–469.
[48] Hu, X. L.; Guo, Y.; Zhang, J. N.; Wang, X. H.; Fang, G. Z.; Wang, S. A signal-amplified ratiometric fluorescence biomimetic sensor based on the synergistic effect of IFE and AE for the visual smart monitoring of oxytetracycline. *Chem. Eng. J.* **2022**, *433*, 134499.
[49] Li, Z. M.; Li, Z. P.; Li, Q. Y.; Xiong, C. M.; Miao, C. Q.; Zhu, B. W.; Zhang, S. B. Dual-centered MOF-on-MOF sensor assisted by molecularly imprinted polymer for rapid and sensitive detection of aflatoxin B1 with dual selectivity mechanism. *Biosens. Bioelectron.* **2025**, *290*, 117933.
[50] Liu, Q.; Zhang, Y. M.; Sun, Q. Q.; Li, H.; Chen, W. M.; Yu, S. R.; Chen, Y. L. High-performance specific detection of NO_2 based on PCN-222-Mn doped with Bi electron mediator. *Sens. Actuators B: Chem.* **2024**, *399*, 134865.
[51] Li, H.; Zhou, L.; Chen, Z. L. Selective removal of oxytetracycline from aquaculture wastewater by molecular imprinting Fe–Co MOF nanosheets. *J. Water Process Eng.* **2025**, *76*, 108133.
[52] Xing, G. W.; Shang, Y. T.; Ai, J. B.; Lin, H. F.; Wu, Z. N.; Zhang, Q.; Lin, J. M.; Pu, Q. S.; Lin, L. Nanozyme-mediated catalytic signal amplification for microfluidic biosensing of foodborne bacteria. *Anal. Chem.* **2023**, *95*, 13391–13399.
[53] Xu, L. P.; Yang, X. G.; Chen, M.; Li, K.; He, J. D.; Tian, D. H.; Lou, Z. Z.; Tan, F. C.; Lai, P. X.; Camposeo, A. et al. Active optical waveguides and metal ion sensors based on nanofibers with aggregation induced emission. *Nano Res.* **2026**, *19*, 94907572.